Received: 14 December 2023 | Revised: 24 June 2024 | Accepted: 2 July 2024

DOI: 10.1002/qj.4823

Quarterly Journal of the Royal Meteorological Society RMetS

RESEARCH ARTICLE

Impacts of free tropospheric turbulence parametrisation on a sheared tropical cyclone

Amethyst A. Johnson[1] | **Juliane Schwendike**[1] | **Andrew N. Ross**[1] | **Adrian Lock**[2] | **John M. Edwards**[2] | **Jeffrey D. Kepert**[3]

[1]Institute for Climate and Atmospheric Research, University of Leeds, Leeds, UK

[2]Met Office, Exeter, UK

[3]Bureau of Meteorology, Melbourne, Australia

Correspondence
Amethyst A. Johnson, Institute for Climate and Atmospheric Research, University of Leeds, Leeds, West Yorkshire, LS2 9JT, UK.
Email: eeajo@leeds.ac.uk

Funding information
Natural Environment Research Council, Grant/Award Number: NE/S007458/1

Abstract

The turbulent transport of momentum, heat, and moisture can impact tropical cyclone intensity. However, representing subgrid-scale turbulence accurately in numerical weather prediction models is challenging due to a lack of observational data. To address this issue, a case study of Hurricane *Maria* was conducted to analyse the influence of different free tropospheric turbulence parametrisations on sheared tropical cyclones. The study used the current Met Office Unified Model (MetUM) parametrisation, as well as a parametrisation scheme with significantly reduced free tropospheric mixing length. Convection-permitting ensemble simulations were performed for both mixing schemes at two initialisation times (four 18-member ensembles in total), revealing an improvement in the intensity forecasts of Hurricane *Maria* when the mixing length was decreased in the free troposphere. By implementing this change, the less diffuse simulations presented a drier mid-level. The resolved downward transport of drier air from the mid-levels into the inflow layer (so-called "downdraft ventilation") was thus more effective in reducing the storm's intensity. In contrast to earlier studies, where decreasing the diffusivity in the boundary layer intensified the storm, we show that decreasing the free tropospheric diffusivity can weaken the storm by enhancing shear-related weakening processes. While this study was performed using the MetUM, the findings highlight the general importance of considering turbulence parametrisation, and show that changes in diffusivity can have different impacts on storm intensity depending on the environment and where the changes are applied.

KEYWORDS

boundary layer, numerical weather prediction, tropical cyclones, turbulence, wind shear

1 | INTRODUCTION

In tropical cyclones, turbulent processes play a contributing role in transporting momentum, moisture, and heat around the storm (Chen *et al.*, 2021c; Rotunno *et al.*, 2009). Due to the large horizontal extent of the tropical cyclone, it is often too computationally expensive to run operational forecasting models at a high enough resolution to capture the small-scale turbulence (Rotunno *et al.*, 2009), warranting the need for turbulence parametrisations. For example, "turbulence-resolving" models such as large-eddy simulations typically run at ≤ 100 m horizontal resolution for tropical cyclone studies (e.g., Rotunno *et al.*, 2009; Chen *et al.*, 2021a; Li & Pu, 2021). In fact, recent work by Chen *et al.* (2021a) suggested that, to resolve turbulent processes in the tropical cyclone boundary layer, horizontal resolutions as low as 10 m may be the most effective. However, despite recent advances in the in situ measurement of turbulent fluxes in tropical cyclones (Cione *et al.*, 2020), such observational data are still rare, which means that it is difficult to develop and test turbulence parametrisations for tropical cyclones in operational forecasting models.

Much of the work on turbulence parametrisation (Chen *et al.*, 2021b, 2021c; Zhang & Rogers, 2019) has focused on turbulence in the boundary layer, and has established that tropical cyclone intensity forecasts are sensitive to the choice of boundary-layer turbulence parametrisation. While many boundary-layer parametrisation schemes only consider vertical diffusion, the horizontal diffusion can also play a role in modulating tropical cyclone intensity forecasts (Rotunno & Bryan, 2012). Varying the choice of turbulence parametrisation in the boundary layer has been shown to impact the intensity forecasts of tropical cyclones directly, with lower diffusivity generally producing a more intense storm with a shallower inflow layer (Gopalakrishnan *et al.*, 2013; Rotunno & Bryan, 2012; Zhang *et al.*, 2017b; Zhang & Marks, 2015). It is common for studies of subgrid-scale turbulence to be conducted on an axisymmetric, idealised vortex, which may be complicated further by increased horizontal diffusion to compensate for the omission of resolved radial mixing.

More recently, the impact of such boundary-layer parametrisations has been tested on a case study of an asymmetric tropical cyclone experiencing moderate vertical wind shear during a period of intensity change (Zhang & Rogers, 2019). Moderate vertical wind shear in the context of tropical cyclones is generally defined as being between 4.5 and 11 $\mathrm{m \cdot s^{-1}}$ (Nguyen *et al.*, 2019; Rios-Berrios & Torn, 2017). The study by Zhang and Rogers (2019) demonstrated results whereby smaller vertical diffusivity leads to a stronger storm. Not only did the reduction in diffusivity impact the intensity, it also produced a more resilient vortex, which limited the tilt, thereby reducing the downdrafts of low-entropy air into the inflow layer (Zhang & Rogers, 2019).

Vertical wind shear is of particular interest due to the import of low-entropy (low θ_e) air into the boundary layer of tropical cyclones, which can weaken the inner core convection. Such air can be imported from the mid-levels (so-called 'downdraft ventilation'–Riemer *et al.*, 2010; Tang & Emanuel, 2012; Alland *et al.*, 2021a; Ahern *et al.*, 2021). In the present study, the mid-levels are defined as the low-θ_e layer, between approximately 2 and 5 km altitude. Alternatively, ventilation can occur from environmental air ('radial ventilation'–Alland *et al.*, 2021b). Deep-layer vertical wind shear (850–200 hPa) can tilt the vortex and can cause the distribution of convection to become more asymmetric (Chen *et al.*, 2006; Corbosiero & Molinari, 2002; Tang & Emanuel, 2012). Convective asymmetries caused by vertical wind shear can excite turbulent eddies in the free troposphere through the production of local shear and buoyancy (e.g., Stull, 1988), further encouraging the downward transport of low-θ_e air into the boundary layer.

Although the impact of diffusivity within the boundary layer has been well documented, there is limited research on the relevance of subgrid turbulence parametrisations within the free troposphere. Operational forecasting models, including that used by the Met Office, use three-dimensional "mixing length" closures to approximate the areal extent of subgrid-scale atmospheric mixing. The mixing length (λ) determines the characteristic scale of turbulence, and the relationship between the parametrised diffusivity and mixing length will be discussed in Section 2. The Met Office will soon be upgrading their standard tropospheric mixing routine in their operational Met Office Unified Model (hereafter MetUM) to include a 3D mixing length reduced by between 1–2 orders of magnitude depending on the operational grid length. Exact details of the current and experimental mixing schemes are detailed in Section 2. Ensuring that the operational MetUM remains robust and effective for forecasting tropical cyclone intensity is one of the main motivations of this work.

The purpose of this study is to evaluate the impact of reduced tropospheric mixing on intensity forecasts of sheared tropical cyclones. We will analyse the decaying phase of Hurricane *Maria*, which was an intense, high-impact tropical cyclone affecting the Atlantic basin in September 2017. The synoptic history of *Maria* is detailed in Section 3.1. *Maria* experienced a period of moderate deep-layer vertical wind shear of around 12 $\mathrm{m \cdot s^{-1}}$ on September 22, 2017 according to both the Statistical Hurricane Intensity Prediction Scheme (SHIPS: DeMaria *et al.*, 2005) and the European Centre for Medium

Range Weather Forecasting (ECMWF) ERA5 reanalysis (Hersbach *et al.*, 2018), which limited the storm's intensity and likely contributed to its weakening. The combination of moderate vertical wind shear and storm weakening raises questions around whether Hurricane *Maria* was subject to vortex tilting and subsequent turbulent processes such as downdraft ventilation. This makes *Maria* an interesting case to investigate sensitivity to the subgrid turbulence parametrisation.

We aim to answer two main questions.

- To what extent does tropospheric mixing influence the intensity forecasts of Hurricane *Maria* (2017) during a period of weakening and moderate to high vertical wind shear?
- How does the choice of subgrid turbulence parametrisation in the free troposphere contribute to the thermodynamic processes associated with weakening tilted tropical cyclones?

The rest of the article is organised as follows. Section 2 will give an overview of the model used and the storm-tracking method applied. Section 3 will begin by exploring the basic storm metrics such as intensity and track, as well as shear-related conditions such as the vortex tilt and vertical shear magnitude. Allowing for some basic evaluation between the observations and ensemble means, these metrics will lay the foundations for the following subsections, in which we will systematically compare the structures of two sets of simulations with different turbulent mixing schemes. Analysis of the asymmetric structures will then lead into the more shear-related aspects of the dynamics, such as the ventilation processes and particularly the differences in entropy. The article will conclude by summarising the significance of the subgrid turbulent mixing and providing suggestions for future tropical cyclone forecasting models.

2 | DATA AND METHODS

2.1 | Met Office Unified Model

The Met Office Unified Model (MetUM) is used in the regional tropical configuration (RA2-T: Bush *et al.*, 2023) to provide retrospective ensemble forecasts for Hurricane *Maria*. The MetUM solves the equations for a deep fully compressible, non-hydrostatic atmosphere (Wood *et al.*, 2014) in a semi-Lagrangian advective framework, with no interactive ocean coupling. The variables and diagnostic outputs are projected onto staggered grids, according to Charney–Phillips staggering (Charney & Phillips, 1953) in the vertical and an Arakawa-C grid (Arakawa & Lamb, 1977) in the horizontal. The regional ensemble is nested in the MetUM global ensemble (MOGREPS-G: Bowler *et al.*, 2008), which has 70 vertical levels up to 80 km altitude and 20-km horizontal resolution. The initial conditions for the unperturbed, deterministic base state are generated using the previous six-hour global forecast and data assimilation using a four-dimensional variational data assimilation method (4DVAR) described by (Rawlins *et al.*, 2007), which is based on the technique of Courtier *et al.* (1994). To generate the perturbations, the global model applies an ensemble transform Kalman filter to the unperturbed deterministic member (Bowler *et al.*, 2008) and each regional ensemble member is initialised from the corresponding global member perturbation.

For this study, each 18-member ensemble is run at a horizontal resolution of 0.04° (approx 4.4 km), with 70 vertical levels up to 40 km. This horizontal resolution means that there are 380 longitude grid points (from −80 to −64.82°E) and 550 latitude grid points (from 16.02 to 37.98°N). By using a domain of this size, we minimise the impacts of the domain boundaries on the storm evolution. The vertical resolution is 10 m near the surface, and it is stretched quadratically with height. The model time step is 60 seconds.

The regional configuration is convection-permitting and uses a series of parametrisations to represent subgrid-scale processes. In representing microphysical processes, the MetUM contains a warm rain parametrisation based on Khairoutdinov and Kogan (2000), which was developed based on marine stratocumulus, extended by Boutle *et al.* (2014a) to allow for subgrid variability. For ice microphysics, we use the parametrisation of Field *et al.* (2007), developed based on midlatitude and tropical ice clouds.

The "boundary layer" scheme of Lock *et al.* (2000) is used to calculate the turbulence across the troposphere. The turbulence parametrisation in unstable boundary layers is determined by a K-profile closure and stable boundary layers are dependent on the Richardson number (Ri), according to

$$K = \lambda^2 S f(Ri), \tag{1}$$

where λ is the mixing length, S is the local vertical wind shear, and $f(Ri)$ is a stability dependence function. Within the boundary layer, λ is determined by the depth of the layer, while in the free troposphere above a background value of 40 m is used. Full details of the scheme can be found in Lock *et al.* (2000). At convection-permitting and finer resolutions, typically used in regional modelling, this scheme is blended, following Boutle *et al.* (2014b), within a three-dimensional Smagorinsky-like closure. The Smagorinsky scheme also uses Equation (1), but with its

mixing length (λ_{max}) given by

$$\lambda_{max} = C_s \times \Delta x, \quad (2)$$

where C_s is a constant (0.2) and Δx is the horizontal resolution of the model (4400 m in this case), thus λ_{max} = 880 m. Within the boundary layer, the blending is dependent on the ratio of the grid size to λ, such that the Lock *et al.* (2000) scheme will be used when the turbulence is entirely subgrid and the Smagorinsky one when it is well resolved.

Here, we focus on the stable free troposphere. Boutle *et al.* (2014b) aimed for the blending to relax towards the Smagorinsky scheme above the boundary layer (in the absence of a well-defined length-scale). Typically, in our cases this means that the 3D mixing length initially drops down to λ = 40 m at the boundary-layer top and then increases to λ_{max} as an exponential function of the ratio of height to grid size. This operational scheme will be referred to as λ_{high}, reflecting the scale of mixing that results from using λ_{max} in the free troposphere.

It seems unphysical that the mid troposphere should have a much higher mixing length than the lower troposphere. Therefore, for the upcoming experiments, λ in the stable free troposphere is set to the background value of 40 m ubiquitously, removing the reliance on grid size. This experiment will hereafter be referred to as λ_{low}. For each of the schemes (λ_{high} and λ_{low}), an ensemble of simulations was run initialised on September 22, 2017 at 0000 UTC (for 120 hours) and on September 23, 2017 at 0000 UTC (for 72 hours, to cover the same time period), which will be referred to as the "earlier" and "later" initialisation times respectively. Each pair of experiments (λ_{high} and λ_{low}) is initialised with the same initial conditions from the respective global ensemble member, so the only change is the mixing length. The primary analysis for this work is based on the earlier initialisation time with the full 120-hour simulation; the ensemble initialised 24 hours later serves to validate the results and strengthen the arguments. For the rest of the article, numerical results and figures will be produced using the earlier (120-hour) simulation, unless specified otherwise. All results presented hereafter have been tested to be robust for both initialisation times.

2.2 | Tropical cyclone track

Storm tracks are calculated using an iterative pressure centroid method following Nguyen *et al.* (2014). The National Oceanic and Atmospheric Administration (NOAA) Best Track from the International Best Track Archive for Climate Stewardship (IBTrACS: Knapp *et al.*, 2010) dataset is used for the "first guess" centre location to initialise the pressure centroid algorithm. To estimate the extent of the storm tilt, the same tracking algorithm is applied to the storm at 1, 2, 7, and 10 km altitude. The tilt is then the distance between the low-pressure centre at both height levels (between 1 and 10 km or 2 and 7 km). This method is similar to those detailed in idealised (Riemer *et al.*, 2010) and full-physics (Ahern *et al.*, 2021) studies of sheared tropical cyclones. While previous work (Riemer *et al.*, 2010) chose to calculate the vortex tilt between 1 and 10 km, we use the 2–7 km tilt for this analysis, to draw closer comparisons to the aircraft observations.

2.3 | Vertical wind shear

The model vertical wind shear is calculated as the vector difference between the area mean winds at 850 and 200 hPa. For consistency with previous studies (e.g., Ahern *et al.*, 2021; Dai *et al.*, 2021; Slocum *et al.*, 2022), along with the widely used SHIPS dataset, we use an environmental wind shear, calculated between 200 and 800 km from the storm centre. Recent idealised simulations (Dai *et al.*, 2021) have shown that the impact of altering the definition of environmental shear is small, but SHIPS uses the 200–800 km radius to limit the impact of an imperfect centre estimate (Slocum *et al.*, 2022). Many previous studies (e.g., Ahern *et al.*, 2021; Riemer *et al.*, 2010; Tang & Emanuel, 2012) use this 850–200 hPa metric, acknowledging that it does not represent the complete vertical structure but is a good general approximation of the environmental deep-layer shear. The radius over which to calculate the shear is more context-dependent and subjective.

2.4 | Distinguishing ensemble intensity divergence points

In Section 3, we will use the minimum sea-level pressure (MSLP) and maximum 10-m tangential wind speed (v) as the basic surface intensity metrics to identify the point at which pairs of simulations begin to "diverge." Although the results presented will not represent intensity bifurcation, there will still be differences in intensity evolution between the simulations. Since the analysis will focus on understanding why this occurs, it is important to identify an "intensity divergence point" for each pair of ensemble members. A "pair" refers to a member from the λ_{high} simulations and the corresponding member from the λ_{low} ensemble. Dynamic and thermodynamic processes occurring after the intensity divergence point may be a consequence of the changing intensities and subsequent stochasticity, so most of the results presented here will be based on the hours preceding the intensity divergence.

Since the wind–pressure relationship is not linear, we choose to combine the aforementioned common intensity metrics to determine a more robust approximation of the intensity divergence times:

$$\Delta_i = -\left(MSLP_{\lambda_{\text{high}}} - MSLP_{\lambda_{\text{low}}}\right) \times \left(v_{\lambda_{\text{high}}} - v_{\lambda_{\text{low}}}\right), \quad (3)$$

where MSLP is in hPa and v is in $\text{m} \cdot \text{s}^{-1}$. The intensity divergence time is defined as occurring when $\Delta_i \geq 25$. This value is small enough to capture genuine intensity divergences but large enough to allow for small variability in the intensity.

The ensemble members are then split into three groups based on the value of their maximum intensity divergence. This decomposition will ensure that the signals of more divergent ensemble members do not dominate the potentially weaker signals produced by less divergent members. The groups were determined as "least" ($25 <= \Delta_i <= 50$), "intermediate" ($50 < \Delta_i <= 100$), and "maximum" ($\Delta_i > 100$). If an ensemble member does not reach the minimum Δ_i of $25\,\text{hPa} \cdot \text{m} \cdot \text{s}^{-1}$, it is removed from the analysis. Of 36 ensemble members (between two initialisation times), six did not qualify. The reason for the removal is that the intensity divergence time is a key component of the analysis. Once Δ_i becomes much lower than 25, it becomes difficult to identify a true intensity divergence point due to the inherent variability of the data. It is important to note that all ensemble members across both initialisation times produce the same overall results discussed in Section 3.1.

2.5 | Model verification

The primary source of model verification comes from the metrics provided by the Extended Best Track (part of IBTrACS: Knapp *et al.*, 2010)—primarily the maximum wind speed, MSLP, track (which allows for approximations of the translational speed), and radius of maximum wind (RMW). These metrics are summarised in Figure 1 and will be discussed in more detail in Section 3.1. Stepped Frequency Microwave Radiometer data (Uhlhorn *et al.*, 2007), collected in aircraft missions operated by NOAA and the United States Air Force, were used independently to verify the RMW from IBTrACS.

Airborne dual-Doppler radar systems (Reasor *et al.*, 2000), known to measure wind speed with high

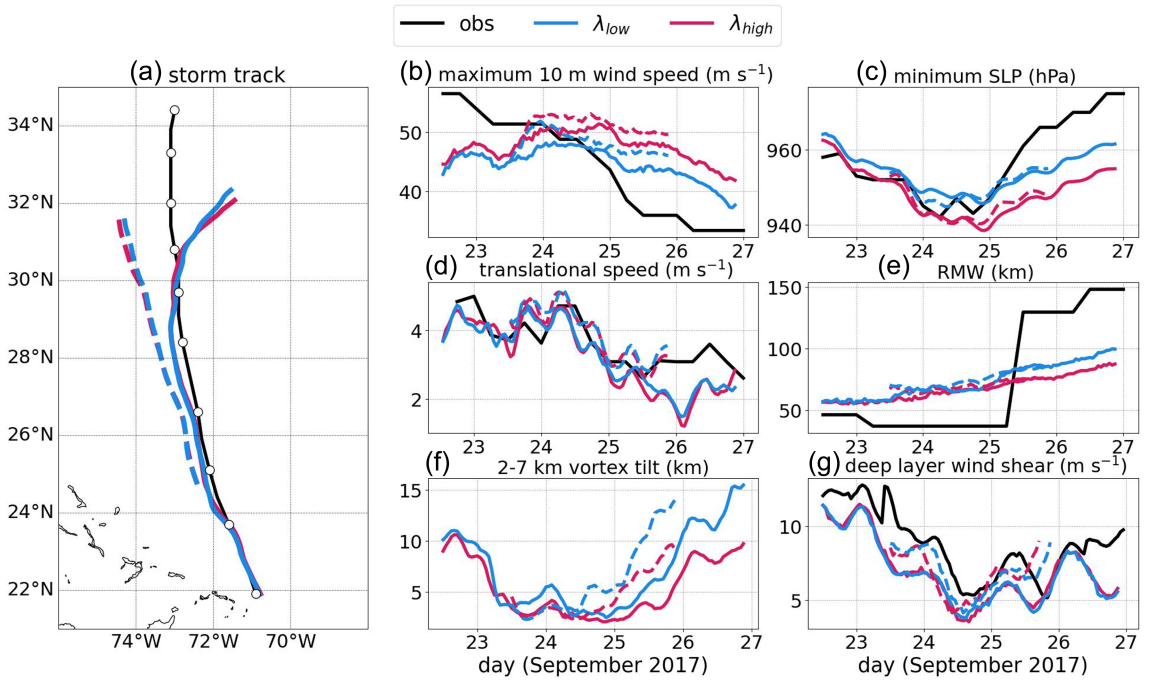

FIGURE 1 Storm metrics of simulations with high (λ_{high}) and low (λ_{low}) free tropospheric mixing length turbulence parametrisations. Solid lines represent the ensemble means for simulations initialised on September 22, 2017 at 0000 UTC, dashed lines represent the ensemble means for the simulations initialised on September 23, 2017 at 0000 UTC. The black lines denote "observations", which are taken from the NOAA Best Track for (a), (b), (c), and (e). The observed translational speed in (d) is calculated from the latitude and longitude values from the Best Track. The deep-layer wind shear in (g) is calculated from the ERA-5 reanalysis dataset, in a 200–800 km annulus from the storm centre. There are not enough data to calculate a time series of observed storm tilt for (f), but observed point values are discussed in Section 3.1. (a) includes white circle markers every 12 hours from September 25, 2017 at 0000 UTC for the Best Track. [Colour figure can be viewed at wileyonlinelibrary.com]

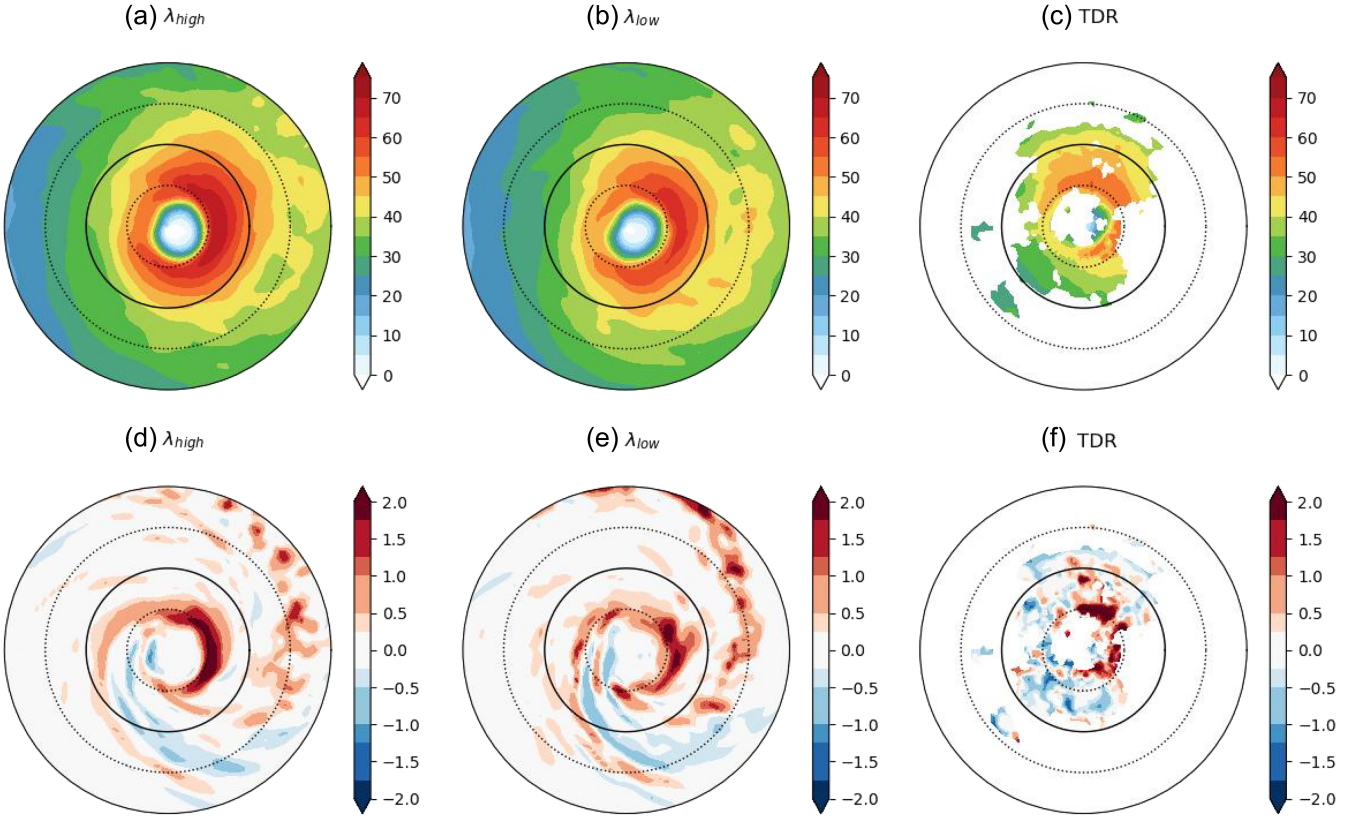

FIGURE 2 A qualitative overview of model performance at $T + 19$ to $T + 23$. (a–c) The tangential wind field at 2-km altitude (filled). (d-f) The vertical velocity field at 2-km altitude (filled). The dotted circles represent 50-km intervals from the storm centre; the solid circle is 100 km. The complete radius is 200 km. The model data (a–d) are produced as a mean from September 22, 2017 1900 and 2300 UTC. The tail Doppler radar fields (c,e) are produced using the flight missions spanning between the same time period. [Colour figure can be viewed at wileyonlinelibrary.com]

accuracy (Lorsolo *et al.*, 2013), provide more information about the three-dimensional storm structure of *Maria*. Figure 2f provides an example of the available data. From these flight missions, NOAA (Fischer *et al.*, 2022) have derived estimations of the 2-km RMW, the 2–7 km tilt, and an approximate storm centre. These plan views are particularly useful for assessing storm asymmetry and evaluating the approximate size of the system, although it is important to note that these are composites produced over approximately four hours from an array of flight passes. In some cases, data are missing or not available due to constraints during the mission and from quality-control procedures.

Global positioning system (GPS) dropsondes were deployed in most of the NOAA flight missions (Aberson *et al.*, 2023). The quality-controlled data were used to validate the model at early forecast times prior to intensity divergence. The data provided by the dropsondes are analysed and used for model evaluation in Section 3.2. In order to evaluate the model against the dropsondes, we approximate the storm centre from the wind-centre fixes calculated from aircraft data (Willoughby & Chelmow, 1982) by the Hurricane Research Division. With a storm centre, it is possible to calculate the radius and azimuth of the sonde. Next, to account for differences in storm size between the model and observations, we normalise by the RMW (r/RMW). For the dropsondes, the RMW is estimated by linear interpolation from the Best Track shown in Figure 1. The process is repeated on the model data (using the track described in Section 2.2) to find the closest relative grid point in the cylindrical coordinate system.

3 | RESULTS AND DISCUSSION

3.1 | Synoptic overview

The study period for this article begins on September 22, 2017 at 0000 UTC and ends on September 27, 2017 at 0000 UTC, which catches the most relevant period of storm weakening, taking place after the initial intensification and just after two major landfalls of Hurricane *Maria*. Throughout the study period, Figure 1a shows that *Maria* moved over the open ocean in a generally north to

northwestward direction, becoming approximately northward moving by September 25. During this period, *Maria* was affected by a deep layer of moderate vertical wind shear (Figure 1g), which was acknowledged in the National Hurricane Center (NHC) report on Hurricane *Maria* (Pasch *et al.*, 2019). While there was a sharp decrease in wind shear between September 23 and 24, *Maria* remained in a state of moderate vertical wind shear throughout the study period and experienced a slow increase in shear after September 24, which likely contributed to tilting the vortex and stunting re-intensification.

Between September 22 and 27, *Maria* gradually began to move more slowly and eventually started to weaken, experiencing a steady decrease in 10-m maximum wind speed, particularly from September 24. While the MSLP remained steady for three days, there was a sharp increase beginning from September 25. *Maria*'s MSLP increase coincided with a sizeable inner-core expansion, going from a surface RMW of less than 40 km to one of over 125 km. The NOAA flight mission 170922H1[1] which occurred approximately between 1900 and 2300 UTC, estimated the 2–7 km tilt to be 13 km, with a RMW at 2-km height of 52.5 km and a maximum wind speed of 46 $m \cdot s^{-1}$. Discrepancies between the tail Doppler radar and Best Track estimates are likely affected by the difference in altitude (surface versus 2-km height) and measurement techniques. It could also be possible that an eyewall replacement cycle took place, which was detected by the airborne radar but not represented by the RMW in the Best Track at this time. Approximately 24 hours later, another NOAA reconnaissance flight mission (170923H1) demonstrated a distinct drop in the 2–7 km tilt, to 3.9 km.

The NOAA flight missions measured rapid increase in the RMW on September 25. Mission 170925H1 operated between approximately 0600 and 1100 UTC and estimated the RMW at 2.5-km height to be 52.5 km. Around 12 hours later, mission 170925H2 estimated the RMW to be 137.50 km.

From September 25, observations of tilt from reconnaissance missions were more sporadic, potentially owing to the lack of useful data swathes and a degradation of the eyewall structure. Between approx 1900 and 0000 UTC, NOAA flight mission 170925H2 estimated a center tilt of 27.3 km, which is still lower than the RMW despite being a sharp increase. The apparent rise in the tilt may be attributed to an increase in vertical wind shear, and could be compounded by a loss of resiliency associated with a substantial increase in the RMW. The official NHC report on Hurricane *Maria* (Pasch *et al.*, 2019) speculated that wind shear was the primary mechanism preventing *Maria* from re-intensifying during this period. It is likely that the wind shear also contributed to Maria's weakening, evidenced by the large observed tilt, which suggests a lack of vortex resiliency. The extent to which vertical wind shear contributed to the weakening of *Maria* will be explored further in the next sections. Another environmental factor that may have contributed to Maria's weakening was the progressively cooler sea-surface temperatures that were encountered as the storm slowly translated northwards (Figure 1a,d). According to the ERA5 reanalysis (Hersbach *et al.*, 2018), by September 24, 2017 at 0000 UTC, the sea-surface temperatures below *Maria* decreased by 4 °C to about 22 °C compared with the start of the simulation (September 22, 0000 UTC). By September 25 at 0000 UTC, the storm entered waters of about 20–21 °C, where the surface temperatures remained approximately constant until the end of the track shown in Figure 1a.

3.2 | Model evaluation

On average, the simulations initiated on September 22 at 0000 UTC followed the observed track well until approximately $T + 96$, on September 25 at 0000 UTC, when the storm began to move eastward in the model and slowed to around 2 $m \cdot s^{-1}$ translation speed. Conversely, in the simulations initiated on September 23 at 0000 UTC, Hurricane *Maria* continued to move more to the west–northwest throughout the study period, continuously increasing the track error.

Every simulation was initiated with a lower wind speed than observed and began to overestimate wind speed within around 48 hours (Figure 1).

The other intensity metric, MSLP, was more similar to the Best Track at the time of initialisation. On average, the ensemble simulations still missed the storm weakening, leading to a lower central pressure than observed. The simulations initialised on September 23 resulted in both a higher MSLP and higher wind speed compared with their September 22 counterpart. Table 1 summarises the average intensity error in each of the simulations. By $T + 72$, the λ_{low} simulations produced storms with noticeably improved intensities compared with the λ_{high} tests. It is important to note that the improvement in the intensity forecast was consistent across every ensemble member and both initialisation times.

In Section 3.1, emphasis was placed on the environment of the storm, particularly the deep-layer wind shear and low sea-surface temperatures, which may have contributed to the weakening of *Maria*. The ensemble simulations produced a moderate deep-layer vertical wind shear (Figure 1g) with a trend consistent with the ERA5 reanalysis and with the official NHC report (Pasch *et al.*, 2019) and a magnitude approximately consistent

TABLE 1 Ensemble averages of minimum sea-level pressure (MSLP; hPa) and maximum 10-m wind speed (u10; $m \cdot s^{-1}$) forecast error and standard deviation for two tropospheric mixing schemes at $T + 72$.

Initialisation time	Run time	SLP error (λ_{high})	SLP error (λ_{low})	u10 error (λ_{high})	u10 error (λ_{low})
Sept 22, 2017 00 Z	120 h	-6.7 ± 7.1	0.5 ± 7.2	6.6 ± 3.7	2.0 ± 4.4
Sept 23, 2017 00 Z	72 h	-16.3 ± 3.8	-9.3 ± 4.0	12.5 ± 2.1	9.5 ± 2.8

to within 1–2 $m \cdot s^{-1}$ on average. Since the modelled storms did not travel as far north as the observed storm (Figure 1a), the sea-surface temperatures were around 1–2 K higher in the simulations by the end of the forecast time, which may have contributed to the less rapid weakening shown in Figure 1b,c.

We use the 2–7 km tilt metric in this study to provide a direct comparison with the NOAA flight reconnaissance observations. The modelled tilt shown in Figure 1f is generally consistent with the flight observations described in Section 3.1. The simulations initialised on September 22 produced an average vortex tilt of approximately 10 km, comparable with the value of 13 km measured in-flight. On September 23, flight missions observed a drop in the vortex tilt to < 5 km, which was captured well on average by all of the ensembles. From September 25, when the observations became less certain for vortex tilt, all of the ensembles showed a notable increase. However, no ensemble member captured the very large tilt of 27.3 km suggested by the NOAA flight missions on September 25, but neither did they produce an RMW larger than 130 km. The highest simulated tilt on September 25 was 10 km, produced by an ensemble member in the λ_{low} test.

Similarly, the observed rapid inner-core expansion discussed in Section 3.1 was not captured by the ensemble means (Figure 1e) but was captured to varying degrees in individual ensemble members. It is likely that the observed storm expansion was linked to the breakdown in the inner-core structure consistent with a weakening storm system. The simulations that produced a more similar intensity to the Best Track by the end of the forecast period (λ_{low}) tended to have a slightly higher surface RMW, although it was still much lower than observed. This discrepancy may be partly attributable to the differences in storm track in Figure 1a, wherein the observed storm moved much further north and encountered cooler waters.

More detailed information on the storm dynamics can be derived from the NOAA reconnaissance flight missions. The tail Doppler radar plan views in Figure 2c,e verified that the simulations were producing storms with low-level tangential and vertical wind fields comparable with the observations. For this analysis, we chose to show ensemble member 14 (initialised on September 22), since this was an ensemble member that exhibited an early intensity divergence that could be attributed with reasonable certainty to changes in the model setup rather than a cascade of stochasticity. At the early initialisation times, all ensemble members looked very similar, so this member should be generally representative of the whole group.

Both sets of experiments (Figure 2a,b and Figure 2c,d) produced similar-looking results, with a reasonable sized eye, RMW, and eyewall compared with the airborne radar in Figure 2c,f. While the distribution of the tangential wind (Figure 2a,b,c) is generally consistent, there are some differences in intensity. The λ_{high} simulation (Figure 2a) shows the highest wind speeds, which is consistent with the general trend shown in Figure 1b. Ideally, the simulations would be evaluated against the radar observations at an earlier forecast time to reduce the impacts of the parametrisation differences; however, this analysis is limited based on observation availability.

The dropsondes provide insight into the vertical structure of the boundary layer and lower troposphere—the results will be described here and are shown in Figure 3. Due to the highly asymmetric nature of tropical cyclones under shear and the limited distribution of dropsondes, it is difficult to get a representative sample. In this analysis, dropsondes were composited by radius and the model was sampled based on the dropsonde radius and azimuth, as explained in Section 2.5, to get the best possible comparison. For the eyewall region—defined for this analysis as being within 0.75–1.25 of the normalised radius (r/RMW)—all of the ensembles produced a mean maximum inflow velocity within 5 $m \cdot s^{-1}$ of the dropsonde throughout the entirety of the simulation time. In both the model and observations, the inflow tends to reach its maximum magnitude of the order of 20–25 $m \cdot s^{-1}$ between 100 and 200 m altitude (Figure 3b,d). On average, the depth of the inflow layer (defined as 10% of the maximum inflow) was consistently overestimated in all sets of simulations by approximately 500 m. There was no apparent change in the depth of the inflow layer between the λ_{high} and λ_{low} experiments.

Where available, eyewall dropsondes within the 12–24 hour period after initialisation (to allow 12 hours for model spin-up) provided a mean maximum tangential wind that was comparable with all sets of ensembles, with an average error of < 4 $m \cdot s^{-1}$, shown in Figure 3a. The height of the maximum tangential wind was overestimated in the simulations by a degree similar to the depth of the inflow layer

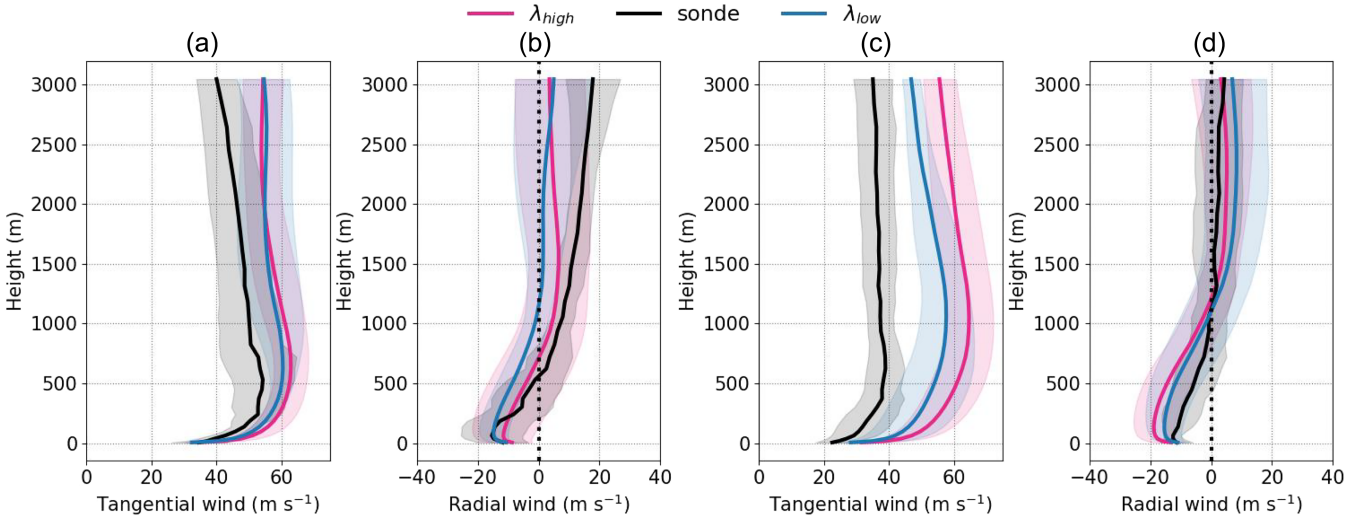

FIGURE 3 Model simulations evaluated against dropsondes, methodology described in the text. (a,b) The tangential and radial wind components respectively (m · s^{-1}) between September 22, 2017, 1200 UTC and September 25, 2017, 0000 UTC. For this period, nine dropsondes were classified as being within the eyewall. (c,d) As in (a,b), but between September 25, 2017, 0000 UTC and September 27, 2017, 0000 UTC, using eight dropsondes. The shaded areas denote the spread. [Colour figure can be viewed at wileyonlinelibrary.com]

(around 500 m). There were no differences in the height of the maximum tangential wind between the experiments across the entire simulation time (Figure 3a,c).

The dropsonde analysis revealed that all of the experiments overestimated the depth of the kinematic (wind-based) boundary layer on average. For example, in Figure 3c the maximum tangential wind in the dropsondes is around 500 m, whereas in the model is it ≈ 1 km.

By the end of the simulation time, the maximum inflow velocity error remained low; however, the tangential wind error grew (Figure 3c,d). The results from the boundary-layer structure support the conclusions from the intensity metrics in Figure 1b, where the maximum 10-m wind-speed error remained higher in the λ_{high} simulations for the entire forecast period. It is useful to analyse intensity metrics from various data sources, since the error is higher in the dropsonde analysis than in the 10-m wind speed for the λ_{high} experiments. Another consideration is that dropsonde soundings are likely to show small-scale features that may not be represented by the model simulations. While averaging over several sondes aims to reduce the signal of this small-scale variability, the ability to represent the general inner-core structure is limited by the small sample size.

3.3 | Asymmetric storm structure

Tropical cyclones experiencing moderate to high vertical wind shear tend to exhibit distinctly asymmetrical structures (Corbosiero & Molinari, 2003), often dominated by the azimuthal wavenumber-1 component (Reasor *et al.*, 2000; Riemer *et al.*, 2010; Zhang *et al.*, 2013). Using the vertical velocity as a proxy for convective regions, the model analysis shows convective asymmetry consistent with idealised models (Riemer *et al.*, 2010) and observational studies (Barron *et al.*, 2022; Hence & Houze, 2012), in which generally convective precipitation occurs in the right-of-shear regions and stratiform rainfall occurs left-of-shear (Figure 2a,b), although this is not ubiquitous across all storm systems (e.g., Tao *et al.*, 2017). The tail Doppler radar (Figure 2; Fischer *et al.*, 2022), shows that the observed structure of *Maria* is consistent with the model simulations at early forecast times ($T \leq 36$). The vertical velocity fields exhibit an azimuthal wavenumber-1 asymmetry, similar to the previous studies.

The distinctly asymmetric structure can be demonstrated by the depth of the inflow layer in Figure 4. During early forecast times, the storm is travelling toward the northwest while encountering a moderate to strong southwesterly vertical wind shear. Figure 4 shows that, at the intensity divergence point for a representative ensemble member, the inflow layer is much deeper in the downshear quadrants compared with the relatively shallow upshear quadrants. These results are supported by a detailed dropsonde composite study (Zhang *et al.*, 2013) which suggests that the downshear right quadrant of sheared tropical cyclones tend to have the deepest inflow layers.

Further analysis (not shown) at later forecast times suggests that the inflow asymmetry changes as time progresses. Once the wind shear weakens, the 530-m model level exhibits inflow ubiquitously across all azimuths. Some symmetry is recovered, although the strongest inflow is still situated downshear. Furthermore, the inflow

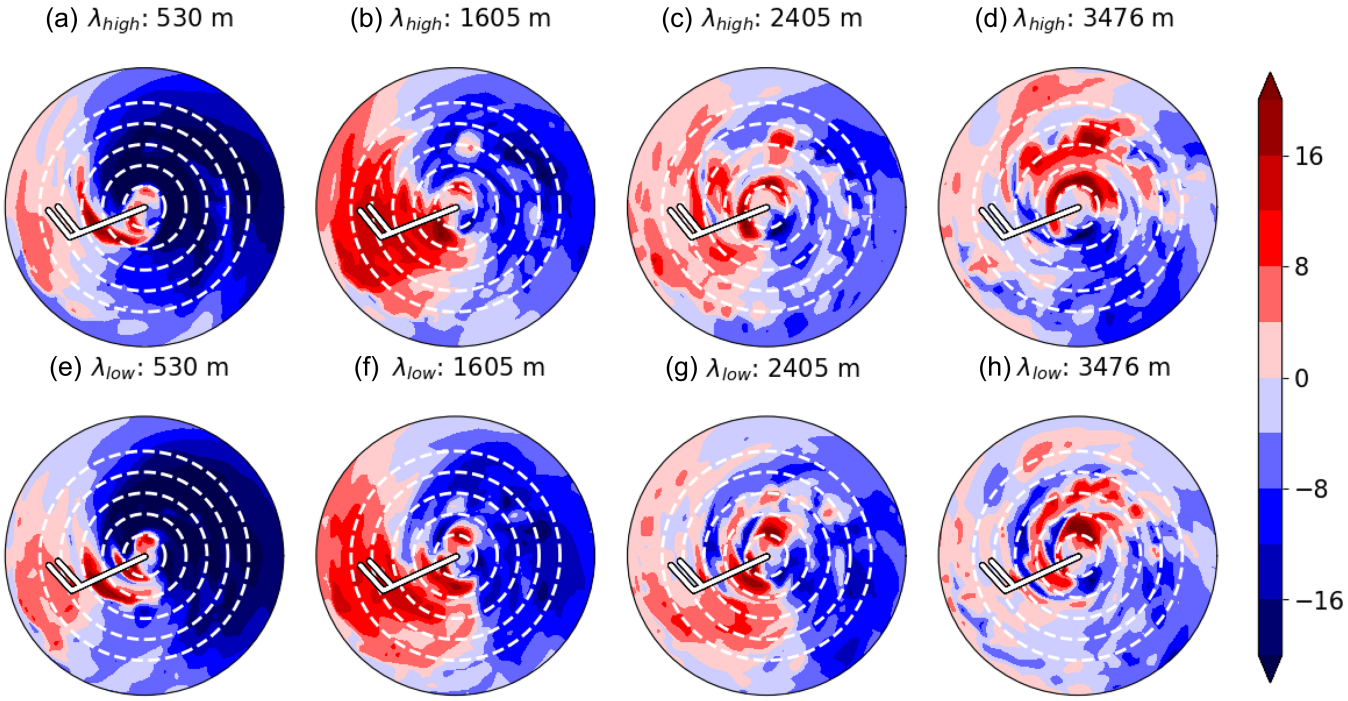

FIGURE 4 Storm-relative radial velocity ($m \cdot s^{-1}$) at the intensity divergence point for a representative ensemble member. The high mixing scheme (λ_{high}) is shown in (a-d); the low mixing scheme (λ_{low}) in (e-h). Dashed contours are at intervals of 25 km radius. The wind barbs represent the deep-layer vertical wind shear. [Colour figure can be viewed at wileyonlinelibrary.com]

layer depth is decreased at these lead times. This may be a reflection of the general storm weakening. In all cases, changing the mixing length (and thus the diffusivity) within the free troposphere produces no discernible change in the inflow layer depth or strength preceding the intensity divergence points.

Previous work, including full-physics modelling (Zhang & Rogers, 2019) and boundary-layer modelling (Kepert, 2012), has investigated the effect of boundary-layer diffusivity on tropical cyclone intensity and structure. In both cases, increased mixing within the boundary layer resulted in a weaker but deeper inflow layer. More specifically, Zhang and Rogers (2019) investigated the effects of increased boundary-layer diffusivity on a sheared tropical cyclone. Along with producing a stronger inflow layer, the storm was also more symmetrical if the boundary-layer diffusivity was reduced. In tandem with the findings presented throughout Section 3, the results given in Zhang and Rogers (2019) show that it is important to consider where the diffusivity is reduced, as changes in the boundary layer versus changes in the troposphere can lead to very different results in terms of storm intensity and resilience to shear. By keeping the boundary-layer mixing the same between the λ_{high} and λ_{low} experiments, we have shown that the free tropospheric mixing can modulate the boundary-layer structure.

3.4 | Vertical mixing

So far, the data analysis we have presented reveals unexpected results, in which more diffusive free tropospheric environments increase the resilience of tropical cyclones against moderate vertical wind shear, ultimately resulting in a more intense tropical cyclone. Zhang and Rogers (2019) found that increasing the eddy diffusivity within the boundary layer produced the opposite effect, in which the more diffuse scheme was less resilient to shear and produced a weaker storm. In the case presented by Zhang and Rogers (2019), the lower boundary-layer diffusivity enhanced low-level convergence, increasing the inflow strength and concentrating the convective bursts to within the RMW. Additionally, Zhang and Marks (2015) identified a stronger eyewall updraft in the low-diffusivity case, linked to the more pronounced vertical gradients of the diabatic heating rate. Since the experiments we conducted only alter the free tropospheric mixing, the boundary-layer convergence is unlikely to be impacted directly, although there may be indirect impacts.

In order to understand these results in the context of the literature, we performed a sensitivity test of ensemble member 14 to evaluate whether vertical or lateral mixing had the biggest impact on the storm intensity (Figure 5). The same model setup was used as described in Section 2, except the lateral mixing was switched off for λ_{high} (hereafter $\lambda_{high,1D}$). For the first 36 hours,

$\lambda_{\text{high,1D}}$ followed almost the exact same MSLP change as its three-dimensional (3D) counterpart, λ_{high}, and diverged from λ_{low} at precisely the same point, which strongly suggests that the primary control is vertical mixing. There is a change in intensification rate between the three-dimensional and $\lambda_{\text{high,1D}}$ simulations during 36–48 hours, which is likely due to stochasticity. Further simulations would be needed to disentangle these effects. Nonetheless, Figure 5 provides strong evidence that the initial divergence is due to changes in vertical mixing.

To evaluate the role of the diffusive moisture fluxes in more detail, the parametrised vertical turbulent moisture flux is shown in Figure 6 and is defined as

$$\overline{w'q_t'} = -K_m \frac{\delta q_t}{\delta z}, \tag{4}$$

where K_m is the diffusivity defined by Equation (1) and q_t is

$$q_t = q_v + q_l + q_f, \tag{5}$$

where q_v is the specific humidity, q_l is the specific liquid water content, and q_f is the specific frozen water content.

Analysis of the vertical turbulent moisture flux in Figure 6 reveals that the diffusivity remains comparable between the simulations within the boundary layer and low-level environment. Regions where the two simulations are statistically significantly ($p < 0.05$) different across a six-hour time period, according to the Wilcoxon Rank Sum Test (Wilcoxon, 1992), are hatched.

There are two main points to take away from Figure 6: the downward flux of moisture is significantly higher in

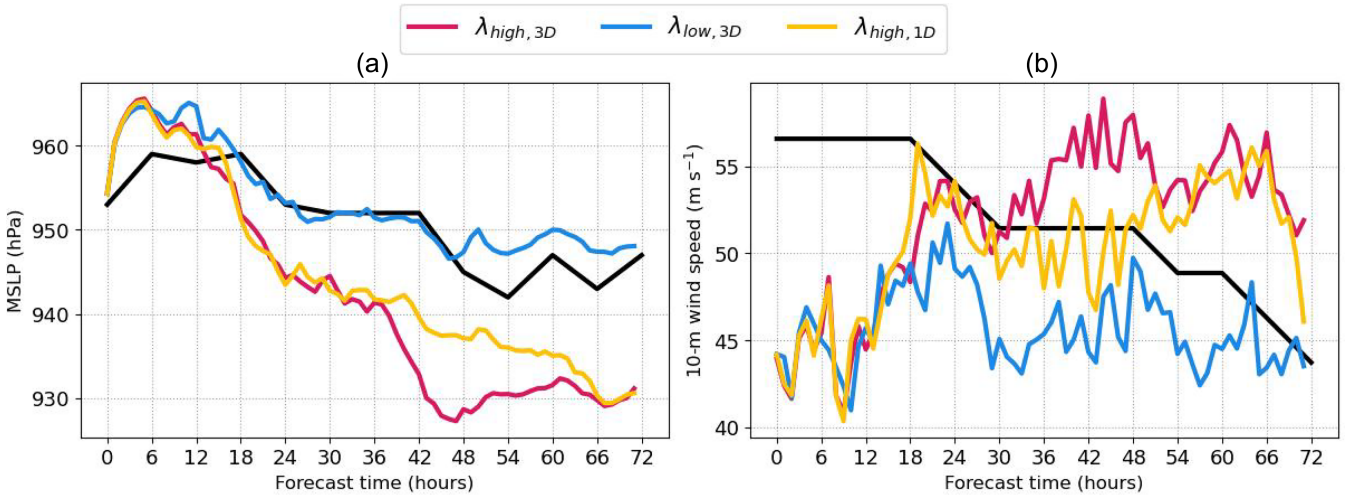

FIGURE 5 (a) Minimum sea-level pressure (hPa). (b) Maximum 10-m wind speed ($m \cdot s^{-1}$). The black line is the NHC best track. $\lambda_{\text{high,3D}}$ corresponds to a simulation with a high three-dimensional mixing length. $\lambda_{\text{low,3D}}$ is the same, but for a reduced mixing length (described in the text). $\lambda_{\text{high,1D}}$ is the same as $\lambda_{\text{high,3D}}$ but with no lateral mixing (only vertical). [Colour figure can be viewed at wileyonlinelibrary.com]

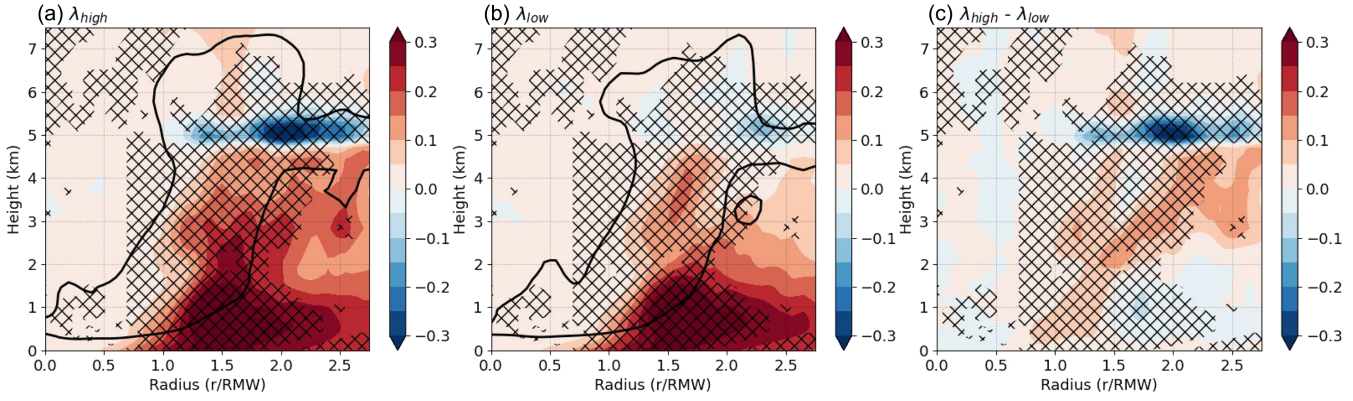

FIGURE 6 Ensemble composite of azimuthally averaged vertical turbulent moisture flux ($\overline{w'q_t'}$) in $g \cdot m^{-2} \cdot s^{-1}$ in two mixing-length (λ) schemes. Negative values (blue) indicate downward transport of moisture. The black solid contour represents the cloud liquid water content at 0.01 $g \cdot kg^{-1}$. The hatching indicates statistical significance in the vertical turbulent moisture flux using the Wilcoxon Rank Sum Test. The composite is averaged over the six hours prior to intensity divergence. The normalised radius is produced using the surface RMW. [Colour figure can be viewed at wileyonlinelibrary.com]

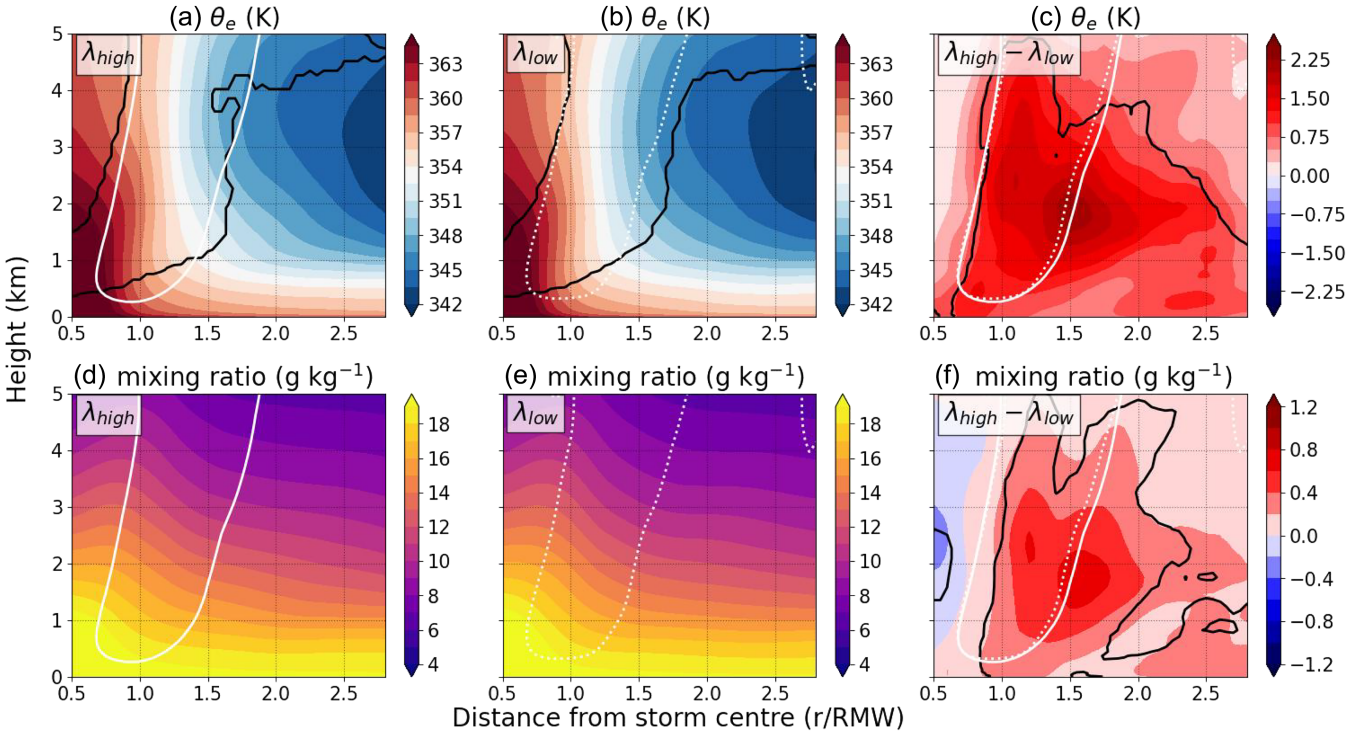

FIGURE 7 Ensemble composites of azimuthally averaged θ_e (K) and mixing ratio (g·kg^{-1}), over a period of 6 hours before intensity divergence. For the θ_e plots in (a) and (b), the black contours indicate a threshold of cloud liquid water cumulative frequency (> 0.001), to provide context about where the cloud layer is. In (c) and (f), the black contours indicate regions of statistically significant difference between the simulations according to a Wilcoxon Rank Sum Test ($p < 0.05$). The unfilled white contours represent vertical velocity $\geq 0.2\,\mathrm{m \cdot s^{-1}}$, for λ_{high} (solid) and λ_{low} (dotted). The radius is normalised by the surface RMW. [Colour figure can be viewed at wileyonlinelibrary.com]

the λ_{high} simulations than in the λ_{low} runs in the main cloud base, and there is also a significantly higher vertical moisture flux in the mid-levels in the λ_{high} runs. Overall, this means that the low-entropy mid-levels are receiving more moisture from the cloud layer and the boundary layer in the λ_{high} simulations, which is consistent with the relatively higher θ_e shown in Figure 7a–c. For the significantly increased upward flux, the λ_{high} simulations reach up to $0.15\,\mathrm{g{\cdot}m^{-2}\cdot s^{-1}}$ higher than their λ_{low} counterparts. For the increased downward flux from the cloud base, the λ_{high} runs are up to $0.25\,\mathrm{g{\cdot}m^{-2}\cdot s^{-1}}$ higher. In the context of a 24-hour period, this can mean a difference of $\approx 13\,\mathrm{kg{\cdot}m^{-2}\cdot day^{-1}}$ more moisture transported upwards from the lower levels into the mid-levels, and $\approx 22\,\mathrm{kg{\cdot}m^{-2}\cdot day^{-1}}$ more moisture transported downward from the cloud layer in the λ_{high} simulations compared with the λ_{low} ensemble members.

Further supporting the idea of increased moisture transport from the cloud layer, Figure 7 shows an ensemble composite of the difference in mixing ratio between λ_{high} and λ_{low}. There is a distinct decrease of moisture in the mid-levels in the λ_{low} members, despite no real change in the inflow characteristics that would indicate either (i) a reduction in the near-surface moisture advection or (ii) an increase in inflow ventilation (the inward transport of dry air from the environment). Since the peak of the moisture change in Figure 7 is along the radially outward edge of the eyewall, where the inflow layer turns into updraft, it is possible that the radial wind has some impact on the moisture flux convergence. However, it is difficult to make this conclusion when the inflow characteristics are very similar between the simulations prior to intensity divergence (e.g., Figure 4), and the moisture is higher throughout the whole lower–mid troposphere in the λ_{high} simulations.

3.5 | Downdraft ventilation

As discussed in Section 1, downdraft ventilation is a process by which low-θ_e (entropy) air can enter the tropical cyclone boundary layer via downdrafts (Alland *et al.*, 2021a; Molinari *et al.*, 2013; Riemer *et al.*, 2010; Tang & Emanuel, 2012; Wadler *et al.*, 2018; Zhang *et al.*, 2017a). These downdrafts are asymmetrically distributed around the tropical cyclone and can be induced by vortex tilting as a result of environmental wind shear (Riemer *et al.*, 2010).

Downdraft ventilation (Figure 10) is calculated using the following equation (Alland *et al.*, 2021a):

$$V = \rho w' \theta_e', \tag{6}$$

where ρ is the air density, w' is the perturbation of downward vertical motion, and θ_e' is the perturbation of equivalent potential temperature (relative to their azimuthal means). Only downward vertical motion is considered for this calculation, ensuring that the ventilation diagnostic is not influenced by convective upward motion such as in the eyewall updraft. For these purposes, the downdraft ventilation is averaged within a 50–150 km radius, which is consistent with the previous study (Alland *et al.*, 2021a). This radius should capture the inner core of the storm effectively without including the impacts of the eye, demonstrated by the RMWs in Figure 1e.

It is likely that Hurricane *Maria* was experiencing downdraft ventilation due to the following evidence. Figure 1g shows that the storm was under the influence of moderate deep-layer vertical wind shear in the MetUM simulations and in the ERA-5 reanalysis, with vortex tilting (Figure 1f) from September 25 aligning well with an increase in MSLP (Figure 1c). The simulations have demonstrated a distinctly asymmetric structure (Section 3.3), with a clear inflow asymmetry that aligns with the shear vectors (Figure 4).

Figure 7 then suggests that there is a difference in the moisture and θ_e profiles between the two simulations, which implies that the downdraft ventilation process may be represented differently between the more diffusive (λ_{high}) and less diffusive (λ_{low}) ensembles.

By increasing the free tropospheric mixing length, the cloud layer can become more diffusive (demonstrated by Figure 6), thus increasing the subgrid-scale vertical moisture transport between the cloud layer and the local environment. By increasing the downward transport of moisture from the cloud layer, the entropy of the mid-levels—where the θ_e minimum typically occurs (Emanuel *et al.*, 1994)—may be increased. This is confirmed by Figure 7, in which all composited ensemble groups display a higher entropy in the λ_{high} simulations.

An important contextual component for this analysis is the presence of a moderate vertical wind shear and wavenumber-1 convective asymmetries discussed in Section 3.3. In environments of moderate wind shear, low-entropy air from the mid-levels can be transported into the boundary layer via downdrafts induced by the asymmetric convective structure (Alland *et al.*, 2021a; Riemer *et al.*, 2010; Tang & Emanuel, 2012; Wadler *et al.*, 2021). Following Riemer *et al.* (2010), a plan view at 1.5 km altitude of the representative ensemble member (Figure 8) suggests that drier air is being drawn further into the inner core in the λ_{low} simulations and is associated with strong ($\leq -0.5\,m \cdot s^{-1}$) downward motion in the left-of-shear quadrants. This result verifies the presence of downdraft ventilation in the simulations and would explain why the boundary layer θ_e has a higher value in the λ_{high} scheme, despite not being directly impacted by the change in the free tropospheric mixing parametrisation.

Although Figure 5 suggests that the primary influence on the intensity change is the vertical mixing, for completeness the radial ventilation (the inward transport of anomalously low θ_e) is also calculated within a 50–150 km radius of the storm centre, according to the following equation from Alland *et al.* (2021b):

$$V_r = \rho u' \theta_e', \tag{7}$$

where u' is the perturbation of inward radial velocity.

Figure 9 shows the radial ventilation in this case, and further confirms the hypothesis that the mid-level θ_e differences (Figure 7) are dominated by the vertical mixing rather than the horizontal mixing. There are higher negative values of ventilation in the λ_{high} simulations below 2 km compared with λ_{low}, which implies the inward transport of anomalously high θ_e. This process, whereby the relatively thermodynamically depleted boundary layer recovers its θ_e through air–sea enthalpy fluxes is referred to as "boundary-layer recovery" (Wadler *et al.*, 2018, 2021). Boundary-layer recovery may explain some of the differences in the low-level θ_e between the simulations but likely has a lower impact on the mid-levels. Note that positive values of radial ventilation suggest the inward transport of anomalously low θ_e, so if radial ventilation were the cause of the mid-level moisture differences in Figure 7, then the λ_{high} simulations might be expected to have lower θ_e. However, since this is not the case, it can be assumed that downdraft ventilation plays the dominant role.

Figure 10 shows the signal of downdraft ventilation in both sets of simulations. From the full field and wavenumber-1 decomposition, shown in Figure 10a,b and Figure 10c,d, it is clear that the downdraft ventilation is at its strongest in the left-of-shear quadrants for both sets of simulations. In the λ_{low} runs, the downdraft ventilation signal peaks around the same altitude as λ_{high} (between 0.5 and 1.5 km), but extends further upward. While this means that the λ_{low} has more ventilation overall, it also suggests that the low-θ_e air in the λ_{low} simulations originates from higher altitudes. From Figure 7 and the associated discussion, in which the θ_e minimum was shown to be approximately 3–4 km, it follows that the penetrating θ_e should be even lower in the λ_{low} simulations than if the ventilation began closer to the boundary layer.

The structure of the wavenumber-1 ventilation signal is similar to an idealised study by Alland *et al.* (2021a), in which the left-of-shear regions are dominated by a positive signal (which has a drying effect) and the right-of-shear regions have a negative signal. Furthermore, the magnitude of the wavenumber-1 component supports the

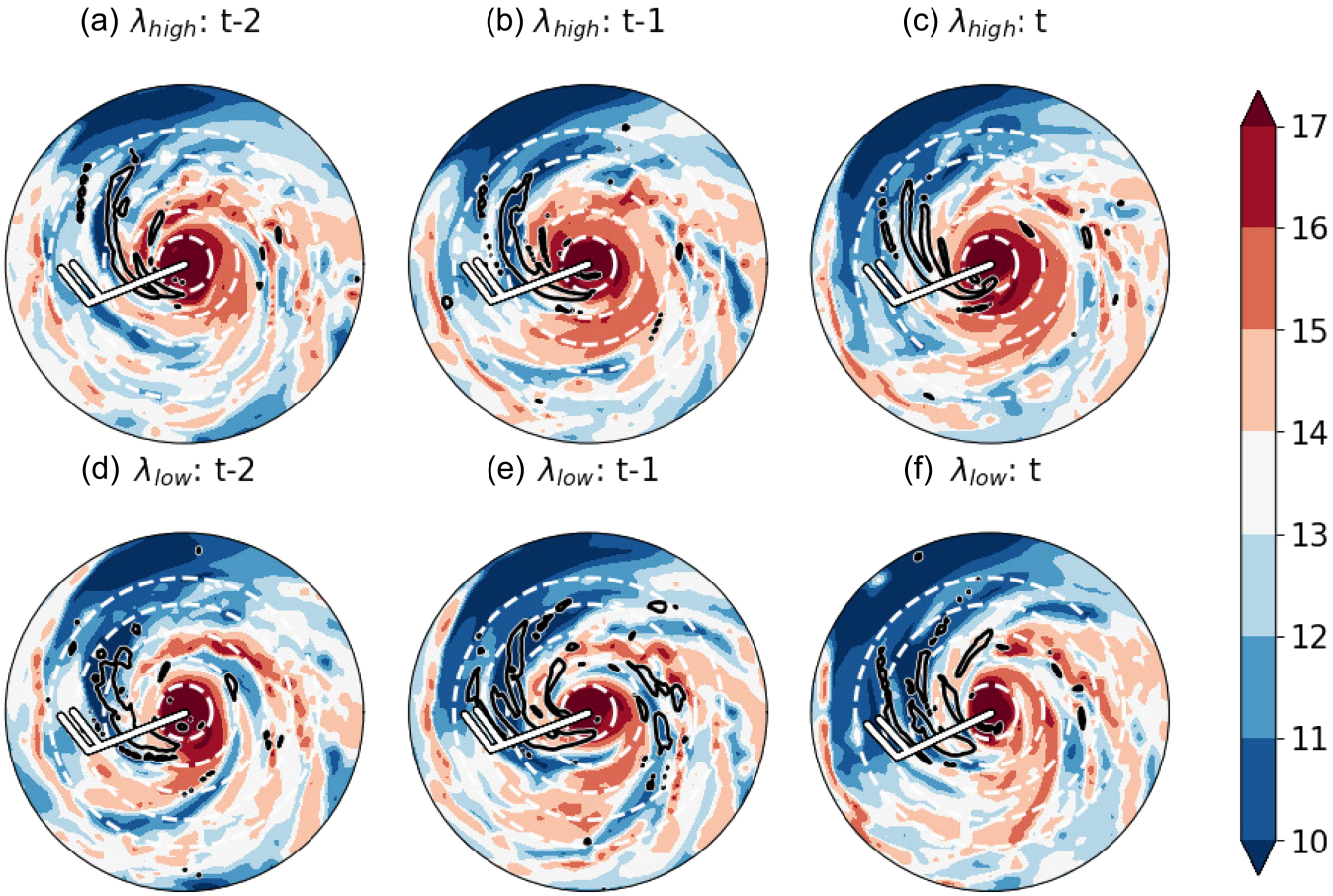

FIGURE 8 Mixing ratio (g·kg^{-1}) at 1.5 km for a representative ensemble member. Black contours indicate downward motion of −0.5 m·s^{-1}. Three simulation times are shown: the time of intensity divergence (t), 1 hour before intensity divergence ($t-1$), and 2 hours before intensity divergence ($t-2$). The deep-layer vertical wind shear is shown as a wind barb. Dashed white lines denote 50-km radius intervals, beginning with 50 km from the storm centre. [Colour figure can be viewed at wileyonlinelibrary.com]

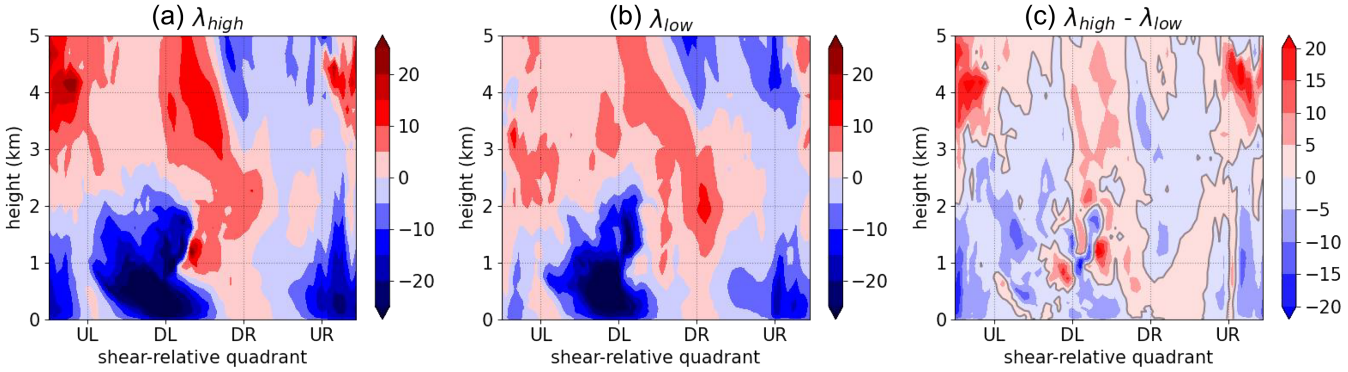

FIGURE 9 An ensemble composite of the radial ventilation in the 6 hours before the intensity divergence point, performed over the inner 50–150 km of the storm. Panels (a) and (b) show the full field of radial ventilation (kg · K · m^{-2} · s^{-1}). (c) The difference between (a) and (b), with the grey line denoting the zero contour. Positive values represent the inward transport of anomalously low θ_e. [Colour figure can be viewed at wileyonlinelibrary.com]

findings of Alland *et al.* (2021a), producing a signal up to about $\pm 3 \times 10^{-1}$ kg · K · m^{-2} · s^{-1}.

The overall structure of the ventilation in Figure 10a,b is also consistent with an observational study by Nguyen *et al.* (2017), which showed that convective downdrafts in the downshear left quadrant can distribute relatively low-θ_e air into the boundary layer, which reduces convection upstream. Nguyen *et al.* (2017) also found

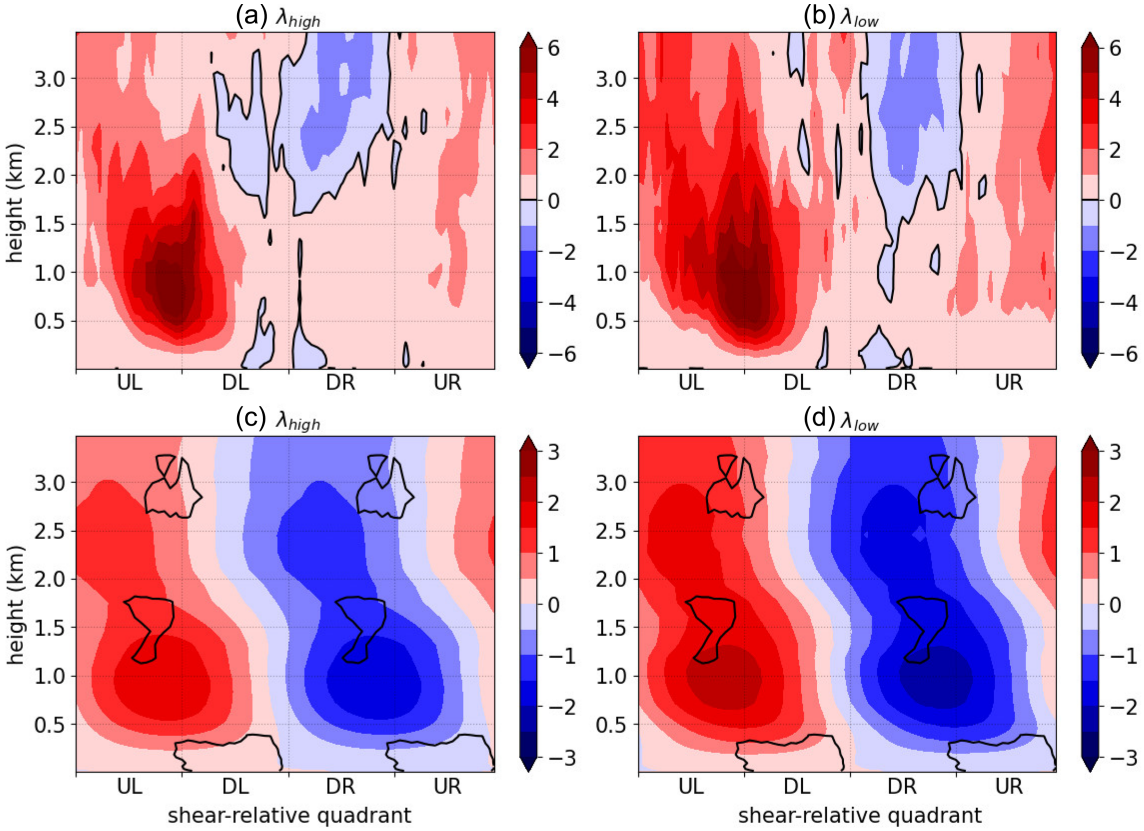

FIGURE 10 An ensemble composite of the downdraft ventilation in the 6 hours before the intensity divergence point, performed over the inner 50–150 km of the storm. Panels (a) and (b) show the full field of downdraft ventilation ($kg \cdot K \cdot m^{-2} \cdot s^{-1}$), where the black contour is the zero line, and panels (c) and (d) show the wavenumber-1 components ($\times 10^{-1}$ $kg \cdot K \cdot m^{-2} \cdot s^{-1}$), where black contours indicate regions of statistically significant ($p < 0.05$) differences between the two simulations. [Colour figure can be viewed at wileyonlinelibrary.com]

that the downdraft ventilation can contribute to storm asymmetries by suppressing convection upstream.

In Figure 10, our results show a much stronger and more widespread downdraft ventilation signal in the λ_{low} simulations, suggesting that there is an increased transport of anomalously low-θ_e air from the mid-levels into the boundary layer. Although the shear is comparable between the simulations (Figure 1g), the λ_{low} simulations seem to be more tilted on average (Figure 1f), which may be contributing to the ventilation differences that we see in Figure 10. In the hours leading up to the intensity divergence point, and between 1.5 and 4 km altitude, there is no significant difference between the strength of the downdrafts between the experiments (Figure 11); however, the downward flux of anomalously low θ_e is significantly higher (t-test; $p < 0.05$) for the λ_{low} simulations. This shows that the ventilation signal is a result of the lower θ_e, rather than a consequence of stronger downdrafts.

Further supporting this point, Figure 11a,b shows that the vertical distribution of the downdrafts is comparable between the λ experiments, but Figure 11d–f demonstrates that the downdrafts tend to have a lower θ_e in the λ_{low} simulations. A two-sample Kolmogorov–Smirnov test, which compares the distribution of two independent samples (Hodges Jr, 1958), showed no significant difference ($p < 0.05$) in the distribution of the vertical motion between the simulations. This evaluation was carried out on averaged groups of ensemble members at 1.5 km altitude, and the test was performed over radial and azimuthal averages independently, to find no significant difference in the radial or azimuthal distribution of vertical motion. Overall, the evidence suggests that the main mechanism of weakening is via a lower θ_e in the low-diffusivity simulation within the downdrafts, rather than the distribution or intensity of the downdrafts being different. Also note that the statistical distribution analysis took the upward motion into consideration too, suggesting no significant difference in the azimuthal or radial distribution of the updrafts before intensity divergence.

When considering Figure 11, it can be seen that there is a slight increase in the incidence of downdrafts $< 0.4\,m \cdot s^{-1}$ in the λ_{low} simulations (Figure 11b). It is likely that these were not picked up by the statistical tests or the probability density function (Figure 11c) due to their low frequency. However, changes in

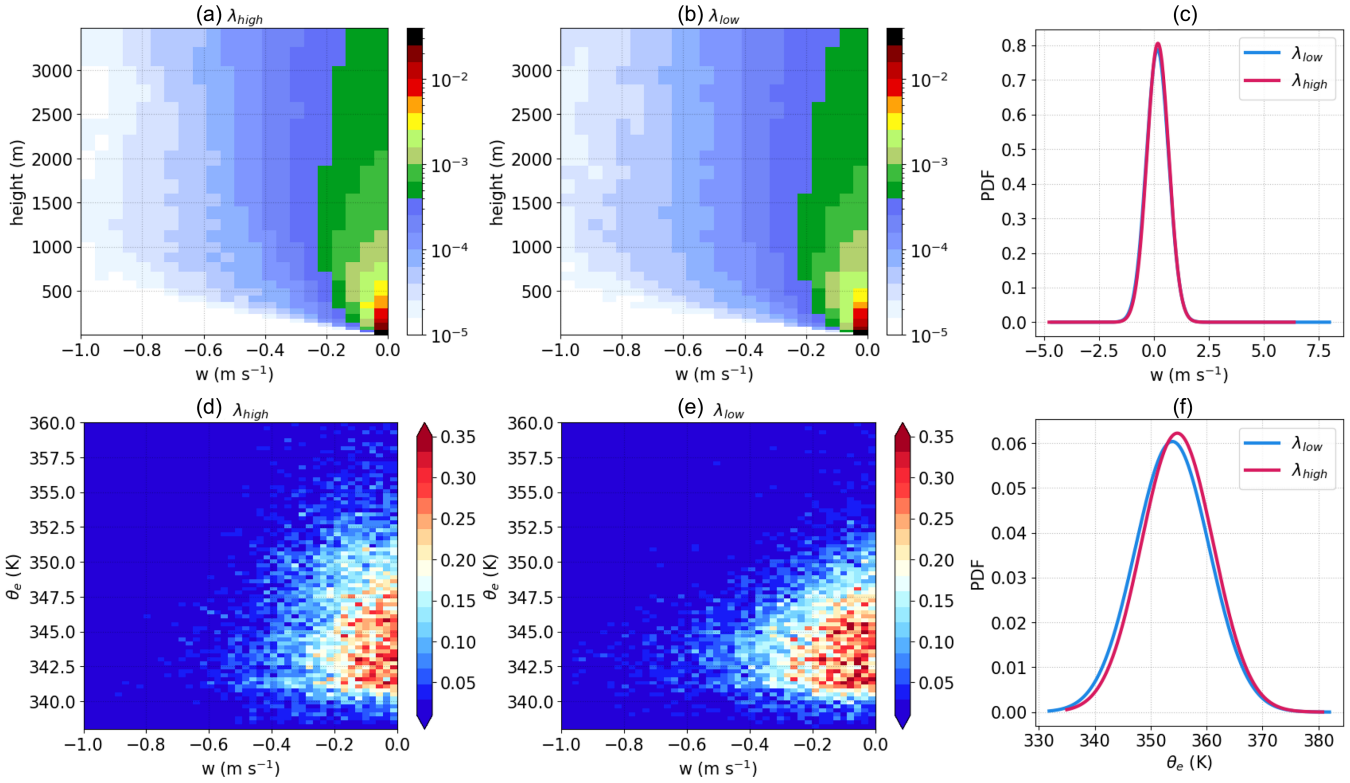

FIGURE 11 An ensemble composite in the six hours before the intensity divergence point, performed at 1-km height over the inner 150 km of the storm, removing the inner 50 km to ensure the results are not skewed by the eye. (a) and (b) are contoured frequency by altitude diagrams of vertical velocity (m · s^{-1}) for the λ_{high} and λ_{low} ensemble members respectively. (d) and (e) are 2D histograms, to show the frequency distribution (K·m · s^{-1}) of θ_e in the downdrafts. (c) and (f) show the probability density function of vertical velocity (m · s^{-1}) and θ_e (K), respectively. [Colour figure can be viewed at wileyonlinelibrary.com]

the strength of the downdrafts are expected to be correlated with θ_e due to the enhanced diabatic cooling. As a result, the simulations would be expected to be more structurally different with increasing time. Stronger downdrafts in the λ_{low} simulations would contribute further to an increased downdraft ventilation.

Since the parcels entering the inflow layer of the λ_{low} scheme have a lower entropy compared with those in the λ_{high} scheme, parcels in the λ_{low} simulations would have to either (i) spend a longer duration in the inflow layer, (ii) have a shallower inflow layer, or (iii) be subject to an inflow layer with stronger entropy fluxes from the sea surface, for the parcels to recover their entropy to the same level as the λ_{high} simulations. If parcels do not recover sufficiently before entering the eyewall region, this could reduce the available potential energy of the eyewall (Tang & Emanuel, 2012), thereby dampening the most convective region of the storm. A study by Yu *et al.* (2023) showed that not only can ventilation impact storm intensity negatively, but it can also have impacts on overall storm structure, leading to more forecast uncertainty. Parcels are more detrimental to the storm's intensity if they enter the inflow layer closer to the eyewall, since, within the outer vicinity of the eyewall, the inflow layer has the maximal potential to recover its entropy from surface fluxes (Wroe & Barnes, 2003), due to the strong secondary circulation reducing the convective vertical mass flux of high-θ_e air out of the boundary layer (Wroe & Barnes, 2003). If a low-θ_e parcel enters the inflow within this region, it can recover its entropy very quickly and may not inhibit eyewall convection (Alland *et al.*, 2021a). Furthermore, Wadler *et al.* (2021) showed that boundary-layer recovery rarely occurs at the top of the inflow layer, so low-entropy downdrafts need to be sufficiently strong to transport air near to the surface.

Alland *et al.* (2021a) showed that parcels entering the inflow layer via downdraft ventilation reduce the convection most effectively when they enter in the upshear regions, where they have the highest chance of reducing the areal extent of vertical motion. It is shown in Figure 10a,b that the λ_{low} simulations have a stronger downdraft ventilation signal in the upshear quadrants than their λ_{high} counterparts, which supports the hypothesis that the downdraft ventilation is a contributing factor to the weaker storm produced by the λ_{low} simulations.

While a parcel trajectory analysis (such as in Alland *et al.*, 2021a; Wadler *et al.*, 2021) would be the most

effective way to prove the hypothesis that λ_{low} parcels that originate from downdrafts tend to enter the eyewall region more thermodynamically depleted than their λ_{high} counterparts, this would require data output at much higher temporal resolution. Instead, we draw from the data presented above. The change in θ_e and moisture (shown in Figure 7a–c and d–f, respectively) peaks at around 2 km, which suggests the change is not surface-driven. There are also no differences in sea-surface temperature between the schemes.

4 | SUMMARY AND DISCUSSION

The main aims of this study were to quantify to what extent tropospheric mixing controls the intensity of Hurricane *Maria* and to establish how the turbulence parametrisation contributes to these intensity-controlling processes. The most robust conclusion from our results is that reducing the tropospheric mixing length (λ) improved the intensity forecast in this case study. While changes were made to the 3D mixing length, sensitivity tests showed that the horizontal component made no significant difference to the simulations and that the primary control was the vertical mixing length. All ensemble members in the λ_{low} experiments produced a lower maximum wind speed and a higher central pressure than their λ_{high} counterparts by the end of the simulation time, which reduced the intensity errors compared with the observed track.

By evaluating the storm environment, it became apparent that *Maria* was under the influence of environmental processes contributing to storm weakening, including reduced sea-surface temperatures and moderate wind shear. In this study, we show that a high vertical mixing length in the mid-levels of tropical cyclones can lead to a higher resolved downward transport of moisture from the cloud layer into the drier low-entropy mid-levels. This moisture subsequently increases the θ_e of the mid-level air. In moderately sheared tropical cyclones, the transport of this low-θ_e air into the boundary layer via resolved convectively induced downdrafts ("downdraft ventilation") is key to stalling intensification or, in some cases, inducing weakening. If the entropy of the mid-levels is greater, then the effectiveness of downdraft ventilation is reduced. We propose that this is part of the reason that the Met Office's operational forecasting model, which used the λ_{high} settings, produced a stronger storm than the Best Track during the forecast period (September 22–27, 2017).

The findings presented here are not in contradiction to the boundary-layer study by Zhang and Rogers (2019), which showed that reduced vertical diffusivity in the boundary layer can produce a more resilient, more intense vortex. Rather, these results complement the previous work by highlighting how the choice of turbulence parametrisation can have different impacts on the storm dynamics based on where the mixing-length changes are applied.

Although the conclusions are robust for Hurricane *Maria*, further work should address the need for more case studies in a diverse set of environments. The primary shear-related processes addressed here (particularly downdraft ventilation) will not be applicable in all tropical cyclones and future research should consider how the tropospheric turbulence parametrisation affects the forecast quality in other stages of the tropical cyclone life cycle. Further work would also benefit from a parcel trajectory analysis, which would require output data of a higher temporal resolution.

Recent changes to the subgrid turbulence parametrisation in the operational MetUM, namely the reduction of the free tropospheric mixing length, are supported by the results presented in this study, in which tropical cyclone intensity forecasts are shown to be improved using a case study of a sheared, weakening tropical cyclone. These results provide confidence that the forecasting quality will be maintained and likely improved by the changes made to the free tropospheric turbulence parametrisation. While this work is based on the MetUM, many operational forecasting models make use of turbulence parametrisations. The results presented here shed light on the importance of free tropospheric turbulence more generally, and should contribute to advances in tropical cyclone modelling.

ACKNOWLEDGEMENTS

We thank the editor, David Nolan, and the two anonymous reviewers who provided valuable, thorough feedback on this article, which led to substantial improvements. This work was supported by the Panorama Natural Environment Research Council (NERC) Doctoral Training Partnership (DTP), under grant NE/S007458/1, with support of Met Office CASE funding. We acknowledge use of the Monsoon2 system, a collaborative facility supplied under the Joint Weather and Climate Research Programme, a strategic partnership between the Met Office and the Natural Environment Research Council. This work was undertaken on ARC4, part of the High Performance Computing facilities at the University of Leeds, UK.

CONFLICT OF INTEREST STATEMENT

There are no conflicts of interest.

DATA AVAILABILITY STATEMENT

The data that support the findings of this study are available from the corresponding author upon reasonable request.

ENDNOTE

[1]The notation of these flight missions is the date (YYMMDD) plus a plane identifier (H; NOAA42 in this case), plus the number of the mission on that day.

ORCID

Amethyst A. Johnson https://orcid.org/0000-0002-2047-1913
Andrew N. Ross https://orcid.org/0000-0002-8631-3512
Adrian Lock https://orcid.org/0000-0001-6289-030X

REFERENCES

Aberson, S.D., Zhang, J.A., Zawislak, J., Sellwood, K., Rogers, R. & Cione, J.J. (2023) The NCAR GPS dropwindsonde and its impact on hurricane operations and research. *Bulletin of the American Meteorological Society*, 104, E2134–E2154.

Ahern, K., Hart, R.E. & Bourassa, M.A. (2021) Asymmetric hurricane boundary layer structure during storm decay. Part I: Formation of descending inflow. *Monthly Weather Review*, 149, 3851–3874.

Alland, J.J., Tang, B.H., Corbosiero, K.L. & Bryan, G.H. (2021a) Combined effects of midlevel dry air and vertical wind shear on tropical cyclone development. Part I: Downdraft ventilation. *Journal of the Atmospheric Sciences*, 78, 763–782.

Alland, J.J., Tang, B.H., Corbosiero, K.L. & Bryan, G.H. (2021b) Combined effects of midlevel dry air and vertical wind shear on tropical cyclone development. Part II: Radial ventilation. *Journal of the Atmospheric Sciences*, 78, 783–796.

Arakawa, A. & Lamb, V.R. (1977) Computational design of the basic dynamical processes of the UCLA general circulation model. *General Circulation Models of the Atmosphere*, 17, 173–265.

Barron, N.R., Didlake, A.C., Jr. & Reasor, P.D. (2022) Statistical analysis of convective updrafts in tropical cyclone rainbands observed by airborne Doppler radar. *Journal of Geophysical Research: Atmospheres*, 127, e2021JD035718.

Boutle, I., Abel, S., Hill, P. & Morcrette, C. (2014a) Spatial variability of liquid cloud and rain: Observations and microphysical effects. *Quarterly Journal of the Royal Meteorological Society*, 140, 583–594.

Boutle, I.A., Eyre, J.E.J. & Lock, A.P. (2014b) Seamless stratocumulus simulation across the turbulent gray zone. *Monthly Weather Review*, 142, 1655–1668. Available from: https://journals.ametsoc.org/view/journals/mwre/142/4/mwr-d-13-00229.1.xml

Bowler, N.E., Arribas, A., Mylne, K.R., Robertson, K.B. & Beare, S.E. (2008) The MOGREPS short-range ensemble prediction system. *Quarterly Journal of the Royal Meteorological Society*, 134, 703–722.

Bush, M., Boutle, I., Edwards, J., Finnenkoetter, A., Franklin, C., Hanley, K. et al. (2023) The second Met Office Unified Model–JULES Regional Atmosphere and Land configuration, RAL2. *Geoscientific Model Development*, 16, 1713–1734. Available from: https://gmd.copernicus.org/articles/16/1713/2023/

Charney, J.G. & Phillips, N. (1953) Numerical integration of the quasi-geostrophic equations for barotropic and simple baroclinic flows. *Journal of Atmospheric Sciences*, 10, 71–99.

Chen, S.S., Knaff, J.A. & Marks, F.D. (2006) Effects of vertical wind shear and storm motion on tropical cyclone rainfall asymmetries deduced from TRMM. *Monthly Weather Review*, 134, 3190–3208.

Chen, X., Bryan, G.H., Zhang, J.A., Cione, J.J. & Marks, F.D. (2021a) A framework for simulating the tropical cyclone boundary layer using large-eddy simulation and its use in evaluating PBL parameterizations. *Journal of the Atmospheric Sciences*, 78, 3559–3574.

Chen, X., Xue, M., Zhou, B., Fang, J., Zhang, J.A. & Marks, F.D. (2021c) Effect of scale-aware planetary boundary layer schemes on tropical cyclone intensification and structural changes in the gray zone. *Monthly Weather Review*, 149, 2079–2095. Available from: https://journals.ametsoc.org/view/journals/mwre/149/7/MWR-D-20-0297.1.xml

Cione, J.J., Bryan, G.H., Dobosy, R., Zhang, J.A., de Boer, G., Aksoy, A. et al. (2020) Eye of the storm: Observing hurricanes with a small unmanned aircraft system. *Bulletin of the American Meteorological Society*, 101, E186–E205. Available from: https://journals.ametsoc.org/view/journals/bams/101/2/bams-d-19-0169.1.xml

Corbosiero, K.L. & Molinari, J. (2002) The effects of vertical wind shear on the distribution of convection in tropical cyclones. *Monthly Weather Review*, 130, 2110–2123.

Corbosiero, K.L. & Molinari, J. (2003) The relationship between storm motion, vertical wind shear, and convective asymmetries in tropical cyclones. *Journal of the Atmospheric Sciences*, 60, 366–376. Available from: https://journals.ametsoc.org/view/journals/atsc/60/2/1520-0469_2003_060_0366_trbsmv_2.0.co_2.xml

Courtier, P., Thépaut, J.-N. & Hollingsworth, A. (1994) A strategy for operational implementation of 4D-Var, using an incremental approach. *Quarterly Journal of the Royal Meteorological Society*, 120, 1367–1387.

Dai, Y., Majumdar, S.J. & Nolan, D.S. (2021) Tropical cyclone resistance to strong environmental shear. *Journal of the Atmospheric Sciences*, 78, 1275–1293.

DeMaria, M., Mainelli, M., Shay, L.K., Knaff, J.A. & Kaplan, J. (2005) Further improvements to the statistical hurricane intensity prediction scheme (SHIPS). *Weather and Forecasting*, 20, 531–543.

Emanuel, K.A. et al. (1994) *Atmospheric Convection*. New York: Oxford University Press.

Field, P.R., Heymsfield, A.J. & Bansemer, A. (2007) Snow size distribution parameterization for midlatitude and tropical ice clouds. *Journal of the Atmospheric Sciences*, 64, 4346–4365.

Fischer, M.S., Reasor, P.D., Rogers, R.F. & Gamache, J.F. (2022) An analysis of tropical cyclone vortex and convective characteristics in relation to storm intensity using a novel airborne Doppler radar database. *Monthly Weather Review*, 150, 2255–2278.

Gopalakrishnan, S.G., Marks, F., Zhang, J.A., Zhang, X., Bao, J.-W. & Tallapragada, V. (2013) A study of the impacts of vertical diffusion on the structure and intensity of the tropical cyclones using the high-resolution HWRF system. *Journal of the Atmospheric Sciences*, 70, 524–541.

Hence, D.A. & Houze, R.A. (2012) Vertical structure of tropical cyclone rainbands as seen by the TRMM precipitation radar. *Journal of the Atmospheric Sciences*, 69, 2644–2661.

Hersbach, H., Bell, B., Berrisford, P., Biavati, G., Horányi, A., Muñoz Sabater, J. et al. (2018) ERA5 hourly data on single levels from 1959 to present. *Copernicus Climate Change Service (C3S) Climate Data Store (CDS)*, 10.

Hodges, J., Jr. (1958) The significance probability of the Smirnov two-sample test. *Arkiv för Matematik*, 3, 469–486.

Kepert, J.D. (2012) Choosing a boundary layer parameterization for tropical cyclone modeling. *Monthly Weather Review*, 140, 1427–1445.

Khairoutdinov, M. & Kogan, Y. (2000) A new cloud physics parameterization in a large-eddy simulation model of marine stratocumulus. *Monthly Weather Review*, 128, 229–243.

Knapp, K.R., Kruk, M.C., Levinson, D.H., Diamond, H.J. & Neumann, C.J. (2010) The international best track archive for climate stewardship (IBTrACS) unifying tropical cyclone data. *Bulletin of the American Meteorological Society*, 91, 363–376.

Li, X. & Pu, Z. (2021) Vertical eddy diffusivity parameterization based on a large-eddy simulation and its impact on prediction of hurricane landfall. *Geophysical Research Letters*, 48, e2020GL090703.

Lock, A.P., Brown, A.R., Bush, M.R., Martin, G.M. & Smith, R.N.B. (2000) A new boundary layer mixing scheme. Part I: Scheme description and single-column model tests. *Monthly Weather Review*, 128, 3187–3199. Available from: https://journals.ametsoc.org/view/journals/mwre/128/9/1520-0493_2000_128_3187_anblms_2.0.co_2.xml

Lorsolo, S., Gamache, J. & Aksoy, A. (2013) Evaluation of the hurricane research division doppler radar analysis software using synthetic data. *Journal of Atmospheric and Oceanic Technology*, 30, 1055–1071. Available from: https://journals.ametsoc.org/view/journals/atot/30/6/jtech-d-12-00161_1.xml

Molinari, J., Frank, J. & Vollaro, D. (2013) Convective bursts, downdraft cooling, and boundary layer recovery in a sheared tropical storm. *Monthly Weather Review*, 141, 1048–1060.

Nguyen, L.T., Molinari, J. & Thomas, D. (2014) Evaluation of tropical cyclone center identification methods in numerical models. *Monthly Weather Review*, 142, 4326–4339.

Nguyen, L.T., Rogers, R., Zawislak, J. & Zhang, J.A. (2019) Assessing the influence of convective downdrafts and surface enthalpy fluxes on tropical cyclone intensity change in moderate vertical wind shear. *Monthly Weather Review*, 147, 3519–3534.

Nguyen, L.T., Rogers, R.F. & Reasor, P.D. (2017) Thermodynamic and kinematic influences on precipitation symmetry in sheared tropical cyclones: Bertha and Cristobel (2014). *Monthly Weather Review*, 145, 4423–4446.

Pasch, R.J., Penny, B.A. & Berg, R. (2019) *Tropical cyclone report: Hurricane Maria (AL152017)*. Tech. rep. Miami: National Hurricane Center.

Rawlins, F., Ballard, S., Bovis, K., Clayton, A., Li, D., Inverarity, G. et al. (2007) The Met Office global four-dimensional variational data assimilation scheme. *Quarterly Journal of the Royal Meteorological Society: A Journal of the Atmospheric Sciences, Applied Meteorology and Physical Oceanography*, 133, 347–362.

Reasor, P.D., Montgomery, M.T., Marks, F.D. & Gamache, J.F. (2000) Low-wavenumber structure and evolution of the hurricane inner core observed by airborne dual-doppler radar. *Monthly Weather Review*, 128, 1653–1680. Available from: https://journals.ametsoc.org/view/journals/mwre/128/6/1520-0493_2000_128_1653_lwsaeo_2.0.co_2.xml

Riemer, M., Montgomery, M.T. & Nicholls, M.E. (2010) A new paradigm for intensity modification of tropical cyclones: Thermodynamic impact of vertical wind shear on the inflow layer. *Atmospheric Chemistry and Physics*, 10, 3163–3188.

Rios-Berrios, R. & Torn, R.D. (2017) Climatological analysis of tropical cyclone intensity changes under moderate vertical wind shear. *Monthly Weather Review*, 145, 1717–1738.

Rotunno, R. & Bryan, G.H. (2012) Effects of parameterized diffusion on simulated hurricanes. *Journal of the Atmospheric Sciences*, 69, 2284–2299.

Rotunno, R., Chen, Y., Wang, W., Davis, C., Dudhia, J. & Holland, G.J. (2009) Large-eddy simulation of an idealized tropical cyclone. *Bulletin of the American Meteorological Society*, 90, 1783–1788. Available from: https://journals.ametsoc.org/view/journals/bams/90/12/2009bams2884_1.xml

Slocum, C.J., Razin, M.N., Knaff, J.A. & Stow, J.P. (2022) Does ERA5 mark a new era for resolving the tropical cyclone environment? *Journal of Climate*, 35, 3547–3564.

Stull, R.B. (1988) *An Introduction to Boundary Layer Meteorology*, Vol. 13. Dordrecht: Springer Science & Business Media.

Tang, B. & Emanuel, K. (2012) A ventilation index for tropical cyclones. *Bulletin of the American Meteorological Society*, 93, 1901–1912.

Tao, C., Jiang, H. & Zawislak, J. (2017) The relative importance of stratiform and convective rainfall in rapidly intensifying tropical cyclones. *Monthly Weather Review*, 145, 795–809.

Uhlhorn, E.W., Black, P.G., Franklin, J.L., Goodberlet, M., Carswell, J. & Goldstein, A.S. (2007) Hurricane surface wind measurements from an operational stepped frequency microwave radiometer. *Monthly Weather Review*, 135, 3070–3085. Available from: https://journals.ametsoc.org/view/journals/mwre/135/9/mwr3454.1.xml

Wadler, J.B., Nolan, D.S., Zhang, J.A. & Shay, L.K. (2021) Thermodynamic characteristics of downdrafts in tropical cyclones as seen in idealized simulations of different intensities. *Journal of the Atmospheric Sciences*, 78, 3503–3524.

Wadler, J.B., Zhang, J.A., Jaimes, B. & Shay, L.K. (2018) Downdrafts and the evolution of boundary layer thermodynamics in hurricane earl (2010) before and during rapid intensification. *Monthly Weather Review*, 146, 3545–3565.

Wilcoxon, F. (1992) Individual comparisons by ranking methods. In: *Breakthroughs in Statistics: Methodology and Distribution*. New York: Springer, pp. 196–202.

Willoughby, H.E. & Chelmow, M.B. (1982) Objective determination of hurricane tracks from aircraft observations. *Monthly Weather Review*, 110, 1298–1305.

Wood, N., Staniforth, A., White, A., Allen, T., Diamantakis, M., Gross, M. et al. (2014) An inherently mass-conserving semi-implicit semi-Lagrangian discretization of the deep-atmosphere global non-hydrostatic equations. *Quarterly Journal of the Royal Meteorological Society*, 140, 1505–1520.

Wroe, D.R. & Barnes, G.M. (2003) Inflow layer energetics of Hurricane Bonnie (1998) near landfall. *Monthly Weather Review*, 131, 1600–1612.

Yu, C.-L., Tang, B. & Fovell, R.G. (2023) Diverging behaviors of simulated tropical cyclones in moderate vertical wind shear. *Journal of the Atmospheric Sciences*, 80, 2837–2860.

Zhang, J.A., Cione, J.J., Kalina, E.A., Uhlhorn, E.W., Hock, T. & Smith, J.A. (2017a) Observations of infrared sea surface temperature and air–sea interaction in hurricane Edouard (2014) using GPS dropsondes. *Journal of Atmospheric and Oceanic Technology*, 34, 1333–1349.

Zhang, J.A. & Marks, F.D. (2015) Effects of horizontal diffusion on tropical cyclone intensity change and structure in idealized three-dimensional numerical simulations. *Monthly Weather Review*, 143, 3981–3995.

Zhang, J.A. & Rogers, R.F. (2019) Effects of parameterized boundary layer structure on hurricane rapid intensification in shear. *Monthly Weather Review*, 147, 853–871.

Zhang, J.A., Rogers, R.F., Reasor, P.D., Uhlhorn, E.W. & Marks, F.D., Jr. (2013) Asymmetric hurricane boundary layer structure from dropsonde composites in relation to the environmental vertical wind shear. *Monthly Weather Review*, 141, 3968–3984.

Zhang, J.A., Rogers, R.F. & Tallapragada, V. (2017b) Impact of parameterized boundary layer structure on tropical cyclone rapid intensification forecasts in HWRF. *Monthly Weather Review*, 145, 1413–1426.

How to cite this article: Johnson, A.A., Schwendike, J., Ross, A.N., Lock, A., Edwards, J.M. & Kepert, J.D. (2024) Impacts of free tropospheric turbulence parametrisation on a sheared tropical cyclone. *Quarterly Journal of the Royal Meteorological Society*, 1–20. Available from: https://doi.org/10.1002/qj.4823